EDGE ARTICLE

Check for updates

All publication charges for this article have been paid for by the Royal Society of Chemistry

A multinitrogen π-conjugated conductive polymer stabilizing ultra-large interlayer spacing in vanadium oxides for high-performance aqueous zinc-ion batteries†

Weijian Li,[ab] Kaiyue Zhu,*[ab] Weikang Jiang,[a] Hanmiao Yang, [ID] [ab] Weili Xie,[ab] Zhengsen Wang[a] and Weishen Yang [ID] *[ab]

Rechargeable aqueous zinc-ion batteries (ZIBs) have attracted increasing attention in the field of electrochemical energy storage (EES) because of their remarkable features, including high theoretical capacity, cost-effectiveness, environmental friendliness, and inherent safety. However, the realization of high-performance cathodes with both high specific capacity and outstanding cycling stability in ZIBs remains challenging. In this work, we present the design of a novel conductive polymer, poly-[2,2′-bipyridin]-5-amine (PBpyA), and report the successful *in situ* intercalation synthesis of PBpyA-intercalated $V_2O_5 \cdot nH_2O$ (designated as PBVO) xerogels. PBVO exhibits exceptional structural stability, attributed to the robust π-conjugation within PBpyA, which effectively stabilizes V_2O_5 bilayers. Moreover, PBVO features a significantly enlarged interlayer spacing of 14.1 Å, facilitating efficient intercalation/extraction of Zn^{2+}. As a cathode material for ZIBs, PBVO demonstrates excellent electrochemical performance, delivering a high specific capacity of 454.6 mA h g^{-1} at 0.1 A g^{-1} and exhibiting remarkable cycling stability, with 97% capacity retention after 150 cycles at 0.2 A g^{-1} and 84% capacity retention after 2000 cycles at 5 A g^{-1}. These findings position PBVO as a highly promising candidate for high-capacity and ultra-stable ZIB cathodes.

Introduction

In recent decades, increasing fossil fuel consumption and the resulting environmental degradation have highlighted the urgent need for sustainable energy technologies such as hydropower, solar, and wind energies.[1] However, the intermittent nature of these renewable sources underscores the necessity for reliable energy storage solutions.[2] Rechargeable batteries, particularly lithium-ion batteries (LIBs), have emerged as promising candidates for integrating renewable sources because of their high energy density and long lifespan.[3] Nonetheless, cost and safety concerns limit their application in large-scale stationary storage, necessitating the development of innovative, secure, and affordable alternatives.[4] Aqueous batteries, with water-based electrolytes, offer an attractive solution by combining safety, affordability, and environmental friendliness.[5] Water-based electrolytes enable fast reaction kinetics, which are crucial for large-scale storage, and eliminate

the safety risks associated with flammable organic electrolytes.[6] Aqueous zinc-ion batteries (ZIBs) leverage earth-abundant Zn metal as the anode, offering advantages such as low cost, high volumetric capacity (5854 mA h cm^{-3})/gravimetric capacity (820 mA h g^{-1}), and a low electrode potential (−0.762 V *vs.* SHE).[7] These features make ZIBs a promising and sustainable energy storage technology.[8]

The performance of ZIBs is strongly influenced by the cathode material.[9] The lack of suitable cathode materials has severely hindered their practical applications, with the challenge lying in designing cathodes that combine high storage capacity with structural robustness to support efficient Zn^{2+} insertion and extraction.[10] To date, various compounds, including manganese-based oxides,[11] vanadium-based oxides,[12] Prussian blue analogues[13] and organic redox-active compounds,[14] have been investigated as potential ZIB cathodes. Among these, vanadium-based oxides have garnered significant attention as potential ZIB cathodes.[15] Multiple oxidation states of V (V^{3+}, V^{4+} and V^{5+}), facile structure distortion, and versatile V–O polyhedral connections[16] contribute to their large theoretical capacity and diverse crystal structures, including layered[17] and tunnel[18] configurations. Layered materials are particularly promising because of their rapid Zn^{2+} transport, with $V_2O_5 \cdot nH_2O$ xerogels standing out due to their

State Key Laboratory of Catalysis, Dalian Institute of Chemical Physics, Chinese Academy of Sciences, Dalian 116023, China. E-mail: yangws@dicp.ac.cn; zky218@dicp.ac.cn

University of Chinese Academy of Sciences, Beijing 100049, China

† Electronic supplementary information (ESI) available. See DOI: https://doi.org/10.1039/d5sc01545f

unique bilayer structure where pillaring water molecules act as a "lubricant" and expand the interlayer spacing (11.5 Å for $n \sim$ 1.6 and 8.7 Å for $n \sim$ 0.5). The enlarged interlayer spacing promoted rapid Zn^{2+} diffusion. However, improving the long-term cycling stability and storage capacity of $V_2O_5 \cdot nH_2O$ is a significant challenge.[19]

A major issue in ZIB systems is the dissolution of vanadium-based materials during electrochemical cycling and electrolyte immersion. This process releases vanadium ions, which react with zinc ions and basic zinc salts to form electrochemically inactive phases such as $Zn_3(OH)_2V_2O_7 \cdot 2H_2O$ (ZOV), leading to capacity degradation.[20] This reaction progressively converts active vanadium species into inactive phases, resulting in a continuous decline in the capacity of the cathode material.[21] Additionally, dissolved vanadium ions may deposit on the anode surface, causing severe passivation and further impairing battery performance. These interrelated degradation mechanisms underscore the need for strategies to suppress vanadium dissolution and enhance the stability of vanadium-based materials. Introducing larger cations (*e.g.*, NH_4^+,[22] Na^+,[23] Ca^{2+},[24] Zn^{2+}[25] and Mg^{2+} (ref. 26)) as interlayer pillars has been explored to improve the cycling stability of $V_2O_5 \cdot nH_2O$ by enlarging the interlayer distance. However, structural degradation during Zn^{2+} insertion and extraction remains a challenge because of the loss of guest ions during cycling. To overcome this, innovative materials with expanded interlayer spacing and improved structural integrity are needed.

Inorganic–organic hybrid materials, such as composites of conductive polymers with cathode materials, have attracted increasing interest in recent years.[27] Conductive polymers with π-conjugated chains (*e.g.*, polypyrrole, polyacetylene, polyaniline, and polythiophene) are widely used in supercapacitors and rechargeable batteries because of their ease of fabrication, controllable structure, flexibility, and high electrical conductivity.[28] When intercalated with $V_2O_5 \cdot nH_2O$, these polymers can significantly enhance cathode performance by (i) enlarging the interlayer spacing for faster Zn^{2+} kinetics, (ii) stabilizing bilayer structures through π-conjugation interactions, and (iii) acting as electron reservoirs to shield electrostatic interactions between Zn^{2+} and the host. Polymers such as polyaniline (PANI)[29] and poly(3,3-ethylenedioxythiophene) (PEDOT)[30] have been used for interlayer expansion of hydrated V_2O_5, but their contributions to capacity and cycling stability remain limited. Designing advanced polymer structures to enhance the performance of these composites is a promising yet challenging research avenue.

In this study, we developed a novel conductive polymer using [2,2′-bipyridine]-5-amine as a monomer and successfully synthesized poly-[2,2′-bipyridin]-5-amine (PBpyA)-intercalated $V_2O_5 \cdot nH_2O$ xerogels (PBVO) *via in situ* intercalation. PBVO, as an innovative ZIB cathode, has exceptional structural stability and exhibits high electrochemical performance. The intercalation of PBpyA significantly enlarges the interlayer spacing, facilitating efficient intercalation/extraction of Zn^{2+}. The bipyridine groups in PBpyA promote Zn^{2+} storage through favourable Zn–N interactions, thus improving the capacity of the cathode. Additionally, the large π-conjugated structure enhances the

crystal stability of V_2O_5 and mitigates electrostatic interactions between Zn^{2+} and the V_2O_5 host. Owing to these features, PBVO achieves a high specific capacity of 454.6 mA h g^{-1} at 0.1 A g^{-1} and outstanding cycling stability, retaining 97% capacity after 150 cycles at 0.2 A g^{-1} and 84% capacity after 2000 cycles at 5 A g^{-1}. These results establish PBVO as a highly promising candidate for high-performance ZIB cathodes and offer a novel design strategy for advanced cathode materials.

Results and discussion

Synthesis and characterization of poly-[2,2′-bipyridin]-5-amine-intercalated $V_2O_5 \cdot nH_2O$

The poly-[2,2′-bipyridin]-5-amine (PBpyA)-intercalated $V_2O_5 \cdot nH_2O$ (PBVO) xerogels were synthesized *via* a one-pot *in situ* hydrothermal reaction by reacting [2,2′-bipyridine]-5-amine monomers with α-V_2O_5 at 150 °C for 3 h (refer to "Synthesis of PBVO" in the Experimental section for details). Under hydrothermal conditions, α-V_2O_5 undergoes dissolution followed by recrystallization, during which the [2,2′-bipyridine]-5-amine (BpyA) monomers are oxidized and polymerized to form polymer chains. These chains are intercalated into the vanadium pentoxide layers, incorporating water molecules and resulting in poly-[2,2′-bipyridin]-5-amine-intercalated $V_2O_5 \cdot nH_2O$ xerogels (Fig. 1a).

The X-ray diffraction (XRD) pattern in Fig. S1† confirms that the absence of water molecules in the interlayers of orthogonal α-V_2O_5. The hydrothermal intercalation of PBpyA transforms orthogonal α-V_2O_5 into a hydrated bilayer V_2O_5 structure (Fig. 1b). As shown in Fig. S2 and S3,† the α-V_2O_5 material retained its orthogonal phase and did not transform to the hydrated bilayer V_2O_5 structure. This demonstrates that polymer intercalation promotes phase transition and enables synthesis under milder conditions. For comparison, the $V_2O_5 \cdot nH_2O$ xerogel without a polymer (H–V_2O_5) was synthesized hydrothermally at 220 °C for 24 hours (Fig. 1b and S4†). XRD patterns (Fig. 1b) confirm that the H–V_2O_5 synthesized at a higher temperature and longer duration shares a similar hydrated layered structure to PBVO. As shown in Fig. 1b, the XRD peak at 6.260° in PBVO, corresponding to the (001) lattice plane of $V_2O_5 \cdot nH_2O$, suggests an enlarged interlayer spacing of 14.1 Å, compared with 11.7 Å in H–V_2O_5. Compared to H–V_2O_5, the expanded interlayer distance in PBVO clearly demonstrated the intercalation of PBpyA into the interlayer spacing of $V_2O_5 \cdot nH_2O$. This expansion facilitates efficient Zn^{2+} intercalation/extraction. The broad, low-intensity XRD peaks corresponding to the (001) lattice plane of PBVO suggest reduced crystallinity due to polymer insertion.

The morphology and particle size of PBVO were examined using scanning electron microscopy (SEM) and transmission electron microscopy (TEM) (Fig. 1c and S5†). SEM images revealed that PBVO consists of layered particles ranging from 1 to 2 μm in size. The high-resolution TEM (HRTEM) image (Fig. 1d) suggest lattice fringes corresponding to the (001) planes with a *d*-spacing of ∼14 Å, confirming that the intercalation of PBpyA into $V_2O_5 \cdot nH_2O$ significantly enlarges the interlayer spacing. Energy-dispersive X-ray spectroscopy (EDS)
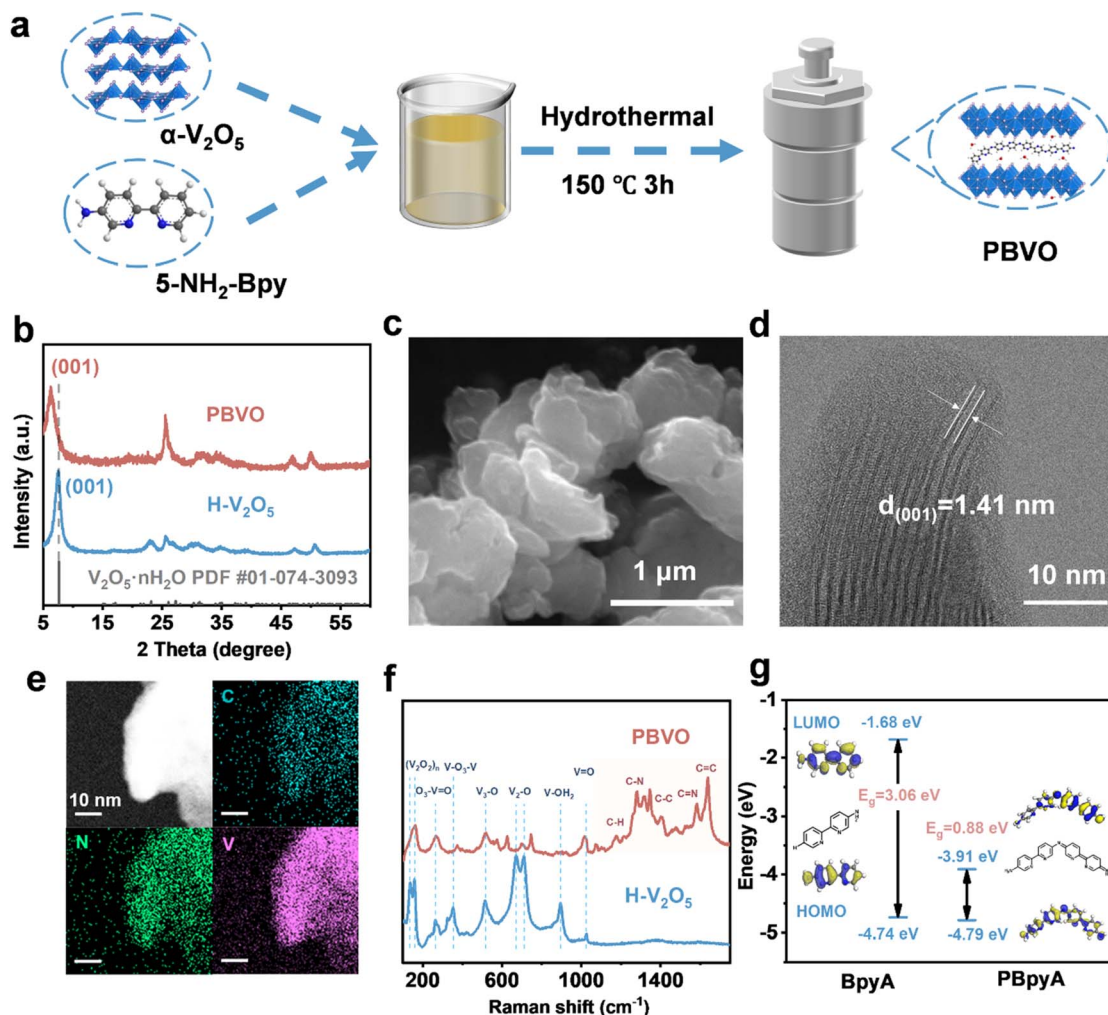
Fig. 1 Structural and morphological characterization of PBVO. (a) Illustration of the synthesis process of PBVO; (b) XRD patterns of PBVO and H−V$_2$O$_5$; (c) SEM image, (d) HRTEM image, and (e) C, N and V elemental mappings of PBVO; (f) Raman spectra of PBVO and H−V$_2$O$_5$; (g) the highest occupied molecular orbital (HOMO) and the lowest unoccupied molecular orbital (LUMO) values of the polymer monomer (BpyA) and bipolymer (PBpyA).

elemental mapping (Fig. 1e and S6†) revealed a uniform distribution of V, O, C, and N in PBVO, confirming successful PBpyA intercalation.

Fourier transform infrared (FT-IR) spectroscopy (Fig. S7†) was used to confirm and analyze the functional groups in the samples. FT-IR spectra demonstrate the successful insertion of PBpyA into the interlayer spaces of V$_2$O$_5$·nH$_2$O. The peaks at 1600–1400 cm^{-1} correspond to pyridine ring stretching, whereas the peaks at 1295 cm^{-1} and 1172 cm^{-1} are attributed to C–N and C–H stretching, respectively. The successful intercalation of PBpyA is also supported by its Raman spectrum (Fig. 1f). The Raman peaks in the range of 1200–1700 cm^{-1} are associated with the organic polymer (including vibrations of C–H, C–N, C–C, C=N, and C=C bonds).

Thermogravimetric analysis (TGA) (Fig. S8†) was employed to quantitatively determine PBpyA and structural water in PBVO. The weight loss of 8.7% below 290 °C is attributed to water evaporation, whereas the 7.5% loss between 290 °C and 420 °C corresponds to PBpyA decomposition. A slight 2.8% mass increase is likely due to the oxidation of low-valent vanadium species (V^{4+}). The PBVO composition is thus estimated to be 7.5% PBpyA/V$_2$O$_5$·nH$_2$O.

Molecular electrostatic potential (ESP) analysis highlights active sites for cation uptake. Notably, nucleophilic and electrophilic centers are associated with regions of higher positive ESP (blue regions) and lower negative ESP (red regions), respectively, as shown in Fig. S9.† The regions near the bipyridine nitrogen and amidogen nitrogen atoms exhibit higher negative ESP values, indicating preferential binding sites for electrophilic cations such as Zn^{2+} and H$^+$ to shield electrostatic interactions between Zn^{2+}/H$^+$ and the host of V–O layers. Density functional theory (DFT) calculations (Fig. 1g) revealed that, compared to its monomer (BpyA), PBpyA has lower HOMO and LUMO values, indicating higher stability and electron affinity. In theory, an extended conjugated structure can reduce the band gap of the LUMO and the HOMO. The narrow energy gap ($\Delta E_{\text{HOMO–LUMO}}$) of the polymer allows facile electron injection and release. In addition, the highly π-conjugated structure

of PBpyA facilitates strong π–d stacking interactions with V–O layers, which are beneficial for maintaining structural integrity and inhibiting the dissolution of V in electrolytes during electrochemical processes.

Electrochemical performance of the PBVO cathode in ZIBs

The cyclic voltammetry (CV) curves were recorded for PBVO as a cathode material in a three-electrode cell ZIB configuration, comprising a Zn foil anode and a Zn ring reference electrode. The first five CV cycles of PBVO, recorded at a scan rate of 0.2 mV s^{-1} between 0.2 and 1.6 V vs. Zn^{2+}/Zn (Fig. 2a), exhibit excellent overlap, indicating outstanding reversibility. During discharge, PBVO accepts electrons from the external circuit, whereas Zn^{2+}/H$^+$ intercalate into the cathode. The nitrogen atoms in the pyridine and imino groups of the PBpyA polymer play a significant role in Zn^{2+}/H$^+$ storage. Upon charging, these ions are extracted from the PBVO structure.

Fig. 2b and c depict the specific discharge/charge capacity curves of PBVO in 2 M Zn(OTf)$_2$ electrolyte at different current densities. PBVO delivers discharge capacities of 454.6 mA h g^{-1}, 390.1 mA h g^{-1}, 347.4 mA h g^{-1}, 313.6 mA h g^{-1}, 280.2 mA h g^{-1}, 241.4 mA h g^{-1} and 200.6 mA h g^{-1} at current densities of 0.1, 0.3, 0.6, 1.2, 2.4, 5, and 10 A g^{-1}, respectively. Remarkably, when the current density returns to 0.3 A g^{-1}, the discharge capacity recovers to its original value, outperforming H–V$_2$O$_5$ and demonstrating excellent rate performance. This superior rate performance is attributed to the expanded interlayer spacing in PBVO, which promotes hydrated zinc-ion diffusion and rapid Zn^{2+} insertion/extraction.

The long-term cycling stabilities of PBVO and H–V$_2$O$_5$ in 2 M Zn(OTf)$_2$ are shown in Fig. 2d, e and S10.† At a current density of 0.2 A g^{-1}, PBVO maintained a specific capacity of 429 mA h g^{-1} with 97% capacity retention after 150 cycles. At a high current density of 5 A g^{-1}, PBVO initially delivers 259 mA h g^{-1}, peaks at 354 mA h g^{-1}, and retains 84% of the peak capacity after 2000 cycles. Comparatively, PBVO outperforms H–V$_2$O$_5$ in terms of both low- and high-current-density stability.

To demonstrate the potential of practical application, the mass loading of cathode was increased from ~1 mg cm^{-2} to ~3 mg cm^{-2}, and the cycling performance of the high-mass-loading cathode was evaluated. The high-mass-loading PBVO electrode also exhibited excellent cycling stability (Fig. S11†), retaining 77% of its peak capacity after 80 cycles, significantly outperforming the high-mass-loading H–V$_2$O$_5$ (retaining 56% after 80 cycles). These results underscore PBVO's promising potential for practical application.

In addition, we evaluated the temperature-dependent electrochemical performance of PBVO at a current density of 0.2 A g^{-1} in the electrolyte of 2 M Zn(OTf)$_2$. As shown in Fig. S12,† PBVO delivered discharge capacities of 546.2, 450.7, 376.6, 308.6, 249.7 and 193.6 mA h g^{-1} at 40 °C, 30 °C, 20 °C, 10 °C, 0 °C and −10 °C, respectively. These results demonstrate that PBVO maintains good electrochemical activity across a wide temperature range, indicating strong adaptability and promising application potential at both high- and low-temperature environments.

In a 2 M ZnSO$_4$ electrolyte, PBVO also demonstrates exceptional cycling stability, with 80% capacity retention after 150 cycles at 0.2 A g^{-1} and 84% capacity retention after 2000 cycles at 5 A g^{-1}, which is superior to that of H–V$_2$O$_5$ (Fig. S13†). The Ragone plot (Fig. S14†) further confirms the competitive electrochemical performance of PBVO relative to that of previously reported materials (Table S1†).[13c,15b,31]
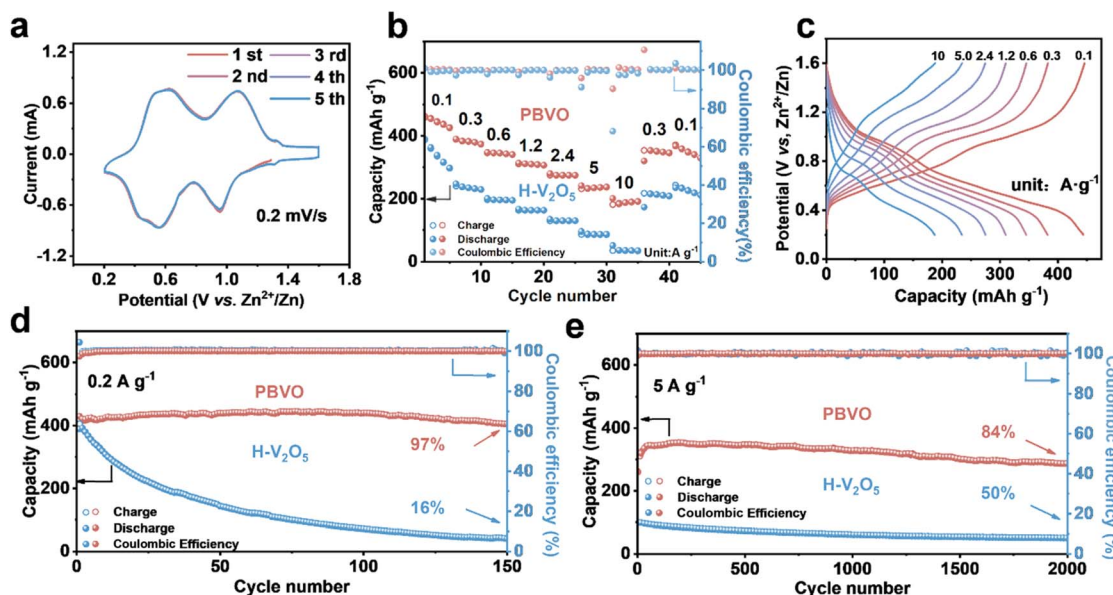

Fig. 2 Electrochemical performance of the PBVO cathode in ZIBs. (a) First five CV curves of the PBVO cathode at a scan rate of 0.2 mV s^{-1} in three-electrode cell configuration ZIBs; (b) rate capability of PBVO and H–V$_2$O$_5$ at various current densities; (c) discharge–charge curves of PBVO at various current densities; (d) cycling performance of PBVO and H–V$_2$O$_5$ at 0.2 A g^{-1}; (e) cycling performance of PBVO and H–V$_2$O$_5$ at 5 A g^{-1}.

The long cycle life of PBVO is attributed to the suppression of irreversible structural damage facilitated by the PBpyA polymer. After soaking in 2 M ZnSO$_4$ for 7 days, the solution containing H–V$_2$O$_5$ turned yellow, whereas the solution with PBVO remained colorless (Fig. S15†).[25,32] Additionally, ICP-OES measurements were conducted to quantitatively analyze the V concentration in electrolytes after soaking PBVO and H–V$_2$O$_5$ for 7 days. The ICP-OES results (Table S2†) revealed that the dissolved vanadium content in ZnSO$_4$ electrolyte after soaking PBVO for 7 days was only 0.180 mmol L^{-1}, threefold lower than that of H–V$_2$O$_5$ (0.603 mmol L^{-1}). This suggests that the highly π-conjugated PBpyA polymer forms robust π–d stacking interactions with V–O layers, effectively preventing vanadium-based material dissolution. The intercalation of conductive polymer confers excellent rate performance and superior structural stability to PBVO. Moreover, the dissolution of vanadium-based materials leads to the formation of the inactive Zn$_3$(OH)$_2$V$_2$O$_7$·2H$_2$O by-product, which contributes to the capacity decay of vanadium-based cathodes.[15a,21]

XRD patterns (Fig. S16†) and SEM images (Fig. S17†) of the PBVO cathode in a fully charged state after 50 cycles at 0.2 A g^{-1} in ZnSO$_4$ show no evidence of Zn$_3$(OH)$_2$V$_2$O$_7$·2H$_2$O formation. In contrast, this by-product with a nanosheet morphology (Fig. S17†) is clearly observed in the H–V$_2$O$_5$ cathode under the same conditions. The intercalation of PBpyA into V$_2$O$_5$·nH$_2$O effectively suppresses the vanadium-based cathode dissolution and prevents the formation of inactive Zn$_3$(OH)$_2$V$_2$O$_7$·2H$_2$O species during cycling, thereby enhancing long-term cycling performance.

Electrochemical kinetics of PBVO in aqueous ZIBs

The electrochemical kinetics of PBVO were investigated via cyclic voltammetry (CV) and electrochemical impedance spectroscopy (EIS) in a three-electrode cell configuration with Zn foil as the anode, a Zn ring as the reference electrode, and 2 M ZnSO$_4$ aqueous electrolyte at room temperature. Fig. 3a shows the CV curves of the PBVO electrode at different scan rates (0.2–1.0 mV s^{-1}) within a potential range of 0.2–1.6 V vs. Zn^{2+}/Zn. The CV curves exhibit consistent shapes and peak positions across scan rates, with two pairs of redox peaks at 1.08/0.95 V and 0.62/0.55 V at 0.2 mV s^{-1}, corresponding to the V^{5+}/V^{4+} and V^{4+}/V^{3+} redox couples, respectively. For comparison, H–V$_2$O$_5$ displays redox peaks at 1.13/0.94 V and 0.81/0.58 V under the same conditions (Fig. S18a†). The obvious shift of peaks between H–V$_2$O$_5$ and PBpyA is likely caused by electron interactions between the intercalated PBpyA polymer and the vanadium oxide layers.

The relationship between the peak current (i) and scan rate (v) is modelled as $i = av^b$, where b determines whether the charge–discharge process is a diffusion-controlled process ($b = 0.5$) or surface-controlled process (capacitive) ($b = 1.0$). Linear fitting of log(i) vs. log(v) yields b values of 0.89, 0.89, 0.82, and 0.86 for PBVO (Fig. 3b) compared with 0.55, 0.79, 0.72, and 0.61 for H–V$_2$O$_5$ (Fig. S18b†). These results indicate a mixed diffusion-controlled and surface-controlled mechanism for PBVO, with a greater capacitive contribution than H–V$_2$O$_5$.

At a constant scan rate, the peak current of the CV curve can be further decomposed into a surface-controlled capacitive process (k_1v) and a diffusion-controlled intercalation process ($k_2v^{1/2}$), expressed as follows:

$$i = k_1v + k_2v^{1/2} \tag{1}$$

Fig. 3c shows that at a scan rate of 0.8 mV s^{-1}, the capacitive contribution of PBVO is approximately 85%, which is significantly greater than that of H–V$_2$O$_5$ (51%) (Fig. S18c†). Across
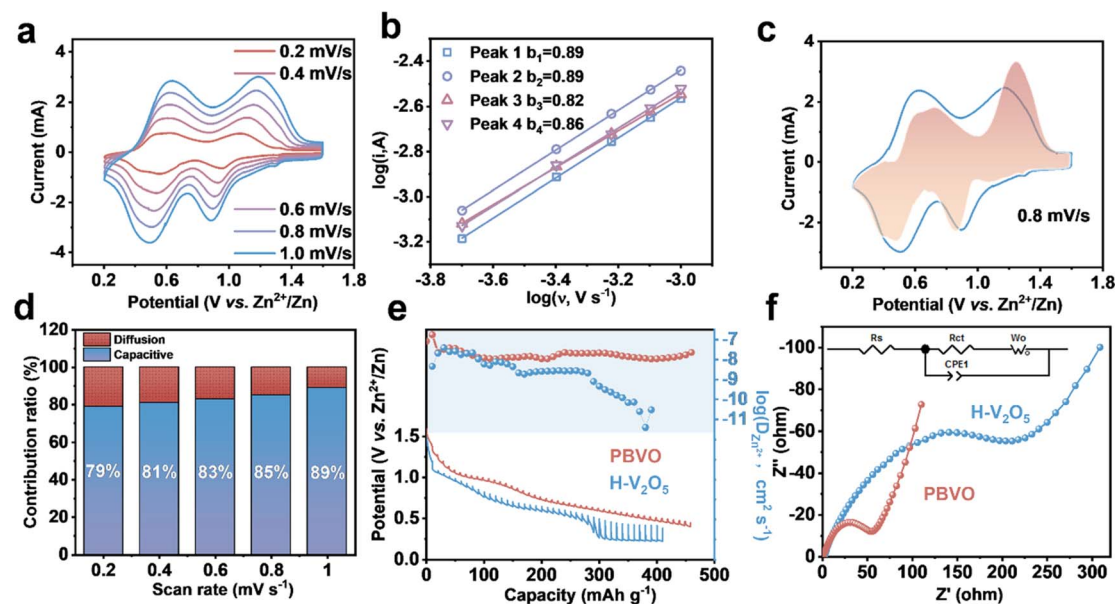

Fig. 3 Kinetic behavior of the PBVO cathode. (a) CV curves at various scan rates; (b) plots of log(peak current) versus log(scan rate); (c) CV curve and the capacitive contribution (pink region) at 0.8 mV s^{-1}; (d) capacity contribution ratios at various scan rates; (e) GITT curves (lower part) at 0.06 A g^{-1} and the corresponding ionic diffusion coefficients of PBVO and H–V$_2$O$_5$; (f) EIS spectra in the OCV state of PBVO and H–V$_2$O$_5$.

scan rates from 0.2 to 1.0 mV s^{-1}, the capacitive contribution of PBVO increases from 79% to 89% (Fig. 3d), whereas that of H–V$_2$O$_5$ increases from 35% to 55% (Fig. S18d†). This highlights the faster ion transport ability and superior rate capability of PBVO.

To understand the kinetic behavior of Zn^{2+} in the cathode, its diffusion coefficient can be obtained *via* the galvanostatic intermittent titration technique (GITT). The diffusion coefficient is calculated as follows:

$$D_{Zn^{2+}}^{GITT} = \frac{4L^2}{\pi\tau}\left(\frac{\Delta E_s}{\Delta E_t}\right)^2 \quad (2)$$

where τ is the constant current pulse time, L is the Zn^{2+} diffusion length (electrode thickness), ΔE_s is the steady-state voltage change during a single-step GITT experiment, and ΔE_t is the cell voltage change at a constant current minus IR-loss during each galvanic step. Fig. 3e and S19† show the discharge/charge curves of the PBVO and H–V$_2$O$_5$ electrodes and the corresponding diffusion coefficients of Zn^{2+} ($D_{Zn^{2+}}$) upon Zn^{2+} insertion and extraction in the electrodes. During the discharge process, the PBVO electrode demonstrated a higher diffusion coefficient of Zn^{2+} (1.74 × 10^{-7} to 1.05 × 10^{-8} cm^2 S^{-1}) than did H–V$_2$O$_5$ (3.86 × 10^{-8} to 3.98 × 10^{-12} cm^2 S^{-1}), confirming that the expanded interlayer spacing of PBVO enhances Zn^{2+} diffusion and facilitates rapid (de)intercalation.

To further elucidate the kinetics of Zn^{2+} transfer at the cathode/electrolyte interface, EIS measurements were performed on PBVO and H–V$_2$O$_5$ electrodes in a three-electrode cell configuration at the open circuit voltage (OCV) after 1 hour of stabilization. Nyquist plots for the PBVO and H–V$_2$O$_5$ electrodes are presented in Fig. 3f, showing a semi-circle in the high-frequency region and a sloping line in the low-frequency region. The calculated charge-transfer resistance (R_{ct}) of PBVO is 59.2 Ω, which is lower than that of the pristine H–V$_2$O$_5$ (241.4 Ω). Additionally, the slope of the low-frequency region for PBVO is steeper than that of H–V$_2$O$_5$, further demonstrating faster ion diffusion in the PBVO electrode.

These findings confirm that PBVO exhibits enhanced electrochemical reaction kinetics due to its large interlayer spacing and the role of the conductive polymer in reducing electrostatic interactions between Zn^{2+} and the V$_2$O$_5$ host.

Electrochemical charging and discharging behavior of PBVO materials

The energy storage mechanism of V-based cathodes in ZIBs is typically associated with the reversible co-intercalation/extraction of Zn^{2+}/H$^+$ during the charging and discharging process. In PBVO, bipyridine nitrogen and amidogen nitrogen atoms within the polymer interact with cations (*e.g.*, Zn^{2+} and H$^+$) during the discharge process (Fig. 4a).
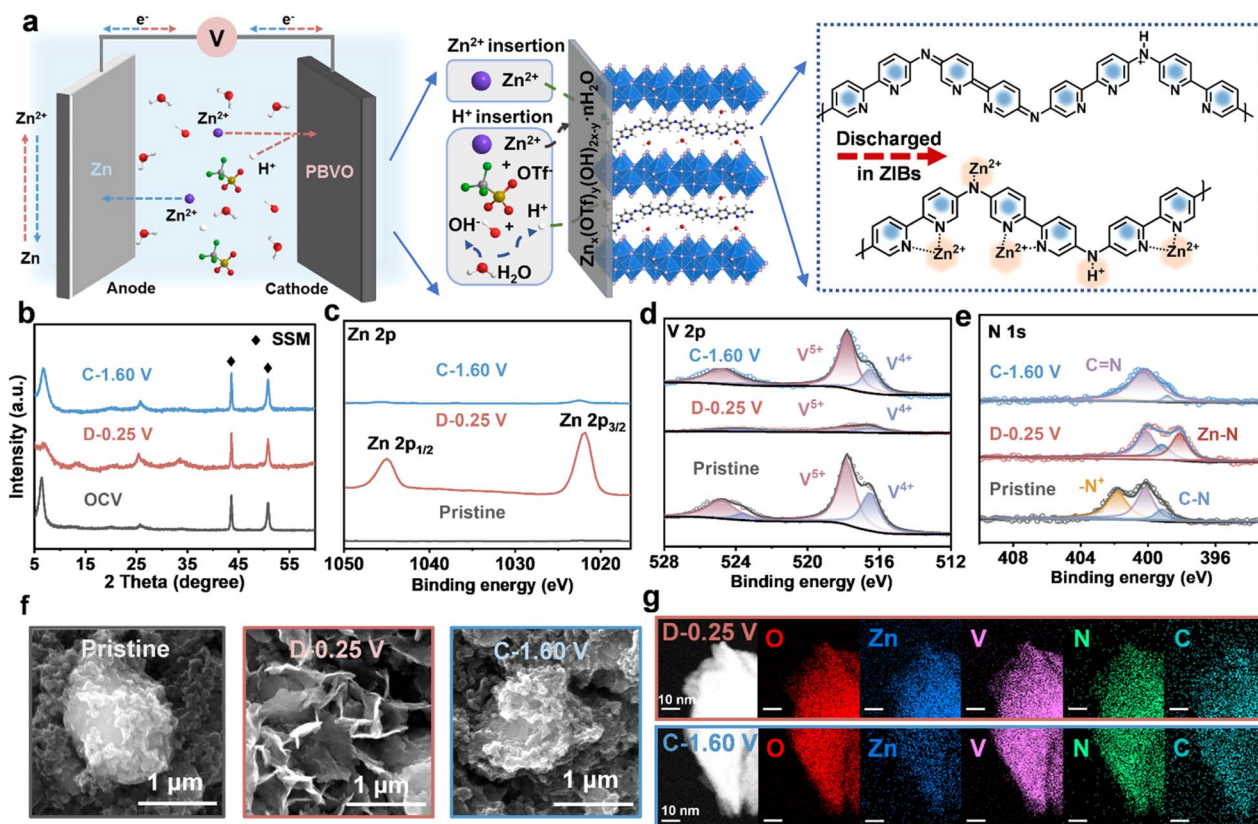

Fig. 4 Compositional analysis of the PBVO cathode in different states at different SOCs (pristine, discharged to 0.25 V and charged to 1.6 V). (a) Illustration of ZIBs and the Zn^{2+}/H$^+$ co-intercalation/extraction mechanism of PBVO; (b) XRD patterns of the PBVO cathode at different SOCs; (c) Zn 2p, (d) V 2p, and (e) N 1s XPS spectra of the PBVO cathode at different SOCs; (f) SEM images of the PBVO cathode at different SOCs; (g) O, Zn, V, N and C elemental mappings of the PBVO cathode at different SOCs.

Ex situ XRD measurements were taken within 1 hour of removing the moist electrode from the cell, allowing us to reasonably capture the structural state. Therefore, *ex situ* XRD achieves comparable accuracy to *in situ* XRD in capturing critical structural evolution. After the first discharge to 0.8 V and 0.25 V, the XRD patterns (Fig. 4b and S20†) show the emergence of new peaks at ~13° and ~33° (broad half-widths), corresponding to the formation of $Zn_x(OTf)_y(OH)_{2x-y} \cdot nH_2O$. These peaks vanish after charging to 0.8 V and 1.6 V, confirming the reversible appearance/disappearance of $Zn_x(OTf)_y(OH)_{2x-y}$-$\cdot nH_2O$ (Fig. 4b, f, S20 and S21†). These results are further supported by the SEM images and the STEM mappings shown in Fig. 4f and g.

Notably, the PBVO electrode in the OCV state was obtained by soaking the PBVO electrode in 2 M $ZnSO_4$ for 3 h and then drying at room temperature (25 °C) for 30 min.

To confirm that H^+ contributes to the capacity in aqueous zinc-ion batteries, we performed the cycling experiment using an aprotic solvent electrolyte (1 M $Zn(CF_3SO_3)_2$ in acetonitrile). PBVO in aprotic solvent electrolyte delivers a capacity of 112 mA h g^{-1} at 0.2 A g^{-1} (Fig. S22†), much lower than that in aqueous electrolyte (429 mA h g^{-1}), directly supporting the contribution of H^+ insertion to the capacity. Regrettably, we are currently unable to quantitatively distinguish the individual contributions of Zn^{2+} and H^+ to the total capacity due to the complex co-intercalation process. Despite its significantly lower concentration relative to Zn^{2+} in aqueous zinc-ion electrolytes, H^+ demonstrates markedly faster intercalation kinetics.[18b,33] Therefore, the intercalation priority of Zn^{2+} and H^+ remains a subject of debate.

Similarly, in a 2 M $ZnSO_4$ electrolyte, PBVO results in the reversible generation and dissolution of basic sulfate ($Zn_4(OH)_6SO_4 \cdot 5H_2O$) (Fig. S23 and S24†), which is also associated with the intercalation/extraction of H^+. This proves that the energy storage mechanism of PBVO in aqueous ZIBs involves the co-insertion of H^+ alongside Zn^{2+}.

To further elucidate the Zn^{2+} storage mechanism of PBVO, *ex situ* XPS was performed at different states of charge (SOCs): pristine, discharged to 0.25 V and charged to 1.6 V (Fig. 4c–e). In the pristine state (Fig. 4c), no Zn is detected. Upon discharging to 0.25 V, peaks at 1022 and 1045.2 eV, corresponding to Zn $2p_{3/2}$ and Zn $2p_{1/2}$, emerge, indicating substantial Zn^{2+} intercalation into the PBVO and deposition on the cathode surface. These Zn signals vanished after charging to 1.6 V, confirming the reversible intercalation/extraction of Zn^{2+} and the appearance/disappearance of $Zn_x(OTf)_y(OH)_{2x-y} \cdot nH_2O$. As shown in Fig. 4d, the peaks at 516.6 eV and 517.8 eV correspond to the V $2p_{3/2}$ of V^{4+} and V^{5+}, whereas the peaks at 523.6 eV and 524.8 eV correspond to the V $2p_{1/2}$ of V^{4+} and V^{5+}. In the pristine state, V exists in a mixed valence state, with partial reduction from V^{5+} because V_2O_5 acts as an oxidant during the *in situ* oxidation of the polymer. In the discharged state (*D*-0.25 V), the V 2p signal is significantly weakened because of the cathode surface coverage by $Zn_x(OTf)_y(OH)_{2x-y} \cdot nH_2O$. However, the relative increase in V^{4+} intensity indicates a redox reaction. After charging to 1.6 V, the V 2p spectra revert to their pristine state, demonstrating that

the vanadium-based material is reversible after the discharge/charge cycle.

Fig. 4e shows the N 1s spectrum of PBVO, in which the peaks located at 401.8 eV, 400.1 eV, 399.2 eV and 398.1 eV correspond to $-N^+$, C–N, C=N and Zn–N bonds, respectively. In the pristine state, nitrogen in the PBpyA polymer is oxidized. Upon discharging to 0.25 V, the polymer undergoes reduction, leading to a decreased nitrogen oxidation state. Concurrently, Zn^{2+}/H^+ coordinated with nitrogen, enhancing the Zn^{2+}/H^+ storage and overall battery capacity. Upon charging to 1.6 V, the polymer reverts to its oxidized state as electrons flow out of the electrode.

The *ex situ* results of XRD, SEM, elemental mapping and XPS clearly reveal that PBVO enables reversible Zn^{2+}/H^+ co-intercalation and extraction. The unique structure and chemical properties of PBVO, including its polymer-hosted conductive network, enable efficient energy storage and redox reversibility during cycling.

Conclusions

In summary, we successfully synthesized a poly-[2,2′-bipyridin]-5-amine (PBpyA)-intercalated $V_2O_5 \cdot nH_2O$ (PBVO) xerogel, demonstrating its remarkable potential as an innovative cathode material for ZIBs. The PBVO cathode exhibited outstanding electrochemical performance, including a high specific capacity of 454.6 mA h g^{-1} at 0.1 A g^{-1} and exceptional cycling stability, with 97% capacity retention after 150 cycles at 0.2 A g^{-1} and 84% capacity retention after 2000 cycles at 5 A g^{-1}. The excellent performances of PBVO are attributed to the following three key factors:

(1) Expanded interlayer spacing. The intercalation of PBpyA significantly increases the interlayer spacing of bilayer V_2O_5 from 11.7 Å to 14.1 Å, enabling fast and reversible Zn^{2+}/H^+ intercalation/extraction.

(2) Enhanced structural stability. The larger π-conjugated structure of the conductive polymer strongly interacts with the V_2O_5 host, reinforcing the crystal structure and improving the cycling stability.

(3) Extra Zn^{2+}/H^+ storage from PBpyA. The coordination between Zn^{2+}/H^+ and nitrogen atoms in the PBpyA polymer facilitates ion storage, leading to an enhancement in the capacity of the cathode.

Furthermore, this work offers a high-performance cathode material and introduces a novel design strategy for cathode materials, advancing the development of aqueous zinc-ion batteries.

Data availability

The data supporting this article have been included as part of the ESI.†

Author contributions

W. Y. and W. L. conceived and designed this work. W. L. and K. Z. collected and analysed data. W. J., H. Y., W. X., and Z. W. assisted in material synthesis and characterization. K. Z.

and W. L. wrote the article. W. Y. revised the article and supervised the project. All authors contributed to the discussion of the results.

Conflicts of interest

There are no conflicts to declare.

Acknowledgements

References

1 S. Chu and A. Majumdar, *Nature*, 2012, **488**, 294–303.

2 (*a*) H. Lund, *Energy*, 2007, **32**, 912–919; (*b*) Z. Yang, J. Zhang, M. C. Kintner-Meyer, X. Lu, D. Choi, J. P. Lemmon and J. Liu, *Chem. Rev.*, 2011, **111**, 3577–3613.

3 Z. Zhu, T. Jiang, M. Ali, Y. Meng, Y. Jin, Y. Cui and W. Chen, *Chem. Rev.*, 2022, **122**, 16610–16751.

4 D. Larcher and J. M. Tarascon, *Nat. Chem.*, 2015, **7**, 19–29.

5 J. O. G. Posada, A. J. R. Rennie, S. P. Villar, V. L. Martins, J. Marinaccio, A. Barnes, C. F. Glover, D. A. Worsley and P. J. Hall, *Renewable Sustainable Energy Rev.*, 2017, **68**, 1174–1182.

6 T. Sun, Q. Nian, X. Ren and Z. Tao, *Joule*, 2023, **7**, 2700–2731.

7 (*a*) M. Song, H. Tan, D. Chao and H. J. Fan, *Adv. Funct. Mater.*, 2018, **28**, 1802564; (*b*) J. Ming, J. Guo, C. Xia, W. Wang and H. N. Alshareef, *Mater. Sci. Eng., R*, 2019, **135**, 58–84; (*c*) J. Zhu, Z. Tie, S. Bi and Z. Niu, *Angew. Chem., Int. Ed.*, 2024, **63**, e202403712; (*d*) Z. Cai, J. Wang and Y. Sun, *eScience*, 2023, **3**, 100093; (*e*) L. Geng, J. Meng, X. Wang, W. Wu, K. Han, M. Huang, C. Han, L. Wu, J. Li, L. Zhou and L. Mai, *Chem*, 2024, **11**, 102302.

8 (*a*) L. Tang, H. Peng, J. Kang, H. Chen, M. Zhang, Y. Liu, D. H. Kim, Y. Liu and Z. Lin, *Chem. Soc. Rev.*, 2024, **53**, 4877–4925; (*b*) K. Zhu, T. Wu, S. Sun, Y. Wen and K. Huang, *ChemElectroChem*, 2020, **7**, 2714–2734.

9 C. Qiu, H. Huang, M. Yang, L. Xue, X. Zhu, Y. Zhao, M. Ni, T. Chen and H. Xia, *Energy Storage Mater.*, 2024, **72**, 103736.

10 (*a*) S. Zuo, X. Xu, S. Ji, Z. Wang, Z. Liu and J. Liu, *Chemistry*, 2021, **27**, 830–860; (*b*) X. Jia, C. Liu, Z. G. Neale, J. Yang and G. Cao, *Chem. Rev.*, 2020, **120**, 7795–7866.

11 (*a*) J. Luan, H. Yuan, J. Liu and C. Zhong, *Energy Storage Mater.*, 2024, **66**, 103206; (*b*) Z. Wang, Y. Fang, J. Shi, Z. Ma, X. Qu and P. Li, *Adv. Energy Mater.*, 2024, **14**, 2303739; (*c*) S. Cui, D. Zhang and Y. Gan, *Adv. Energy Mater.*, 2024, **14**, 2302655; (*d*) S. Wang, S. Yao, N. Dai, W. Fu, Y. Liu, K. Ji, Y. Ji, J. Yang, R. Liu, X. Li, J. Xie, Z. Yang and Y. M. Yan, *Angew. Chem., Int. Ed.*, 2024, **63**, e202408414.

12 (*a*) F. Wan and Z. Niu, *Angew. Chem., Int. Ed.*, 2019, **58**, 16358–16367; (*b*) W. Jiang, K. Zhu and W. Yang, *Chemistry*, 2023, **29**, e202301769; (*c*) P. Hu, P. Hu, T. D. Vu, M. Li, S. Wang, Y. Ke, X. Zeng, L. Mai and Y. Long, *Chem. Rev.*, 2023, **123**, 4353–4415; (*d*) Y. Cui, Y. Ding, L. Guo, Y. Liu, Y. Bai, G. Li and K. Wang, *Energy Mater.*, 2023, **3**, 300023.

13 (*a*) M. Zhang, W. Zhao, T. Yang, R. Gao, D. Luo, H. W. Park, Y. Hu and A. Yu, *Adv. Energy Mater.*, 2024, **14**, 2400543; (*b*) G. Yang, Z. Liang, Q. Li, Y. Li, F. Tian and C. Wang, *ACS Energy Lett.*, 2023, **8**, 4085–4095; (*c*) L. Zhang, L. Chen, X. Zhou and Z. Liu, *Adv. Energy Mater.*, 2014, **5**, 1400930; (*d*) J. Wang, Z. Hu, Y. Qi, C. Han, K. Zhang and W. Li, *J. Mater. Sci. Technol.*, 2025, **221**, 302–320.

14 Y. Chen, K. Fan, Y. Gao and C. Wang, *Adv. Mater.*, 2022, **34**, e2200662.

15 (*a*) K. Zhu and W. Yang, *Acc. Chem. Res.*, 2024, **57**, 2887–2900; (*b*) K. Zhu, T. Wu and K. Huang, *Adv. Energy Mater.*, 2019, **9**, 1901968.

16 P. Y. Zavalij and M. S. Whittingham, *Acta Crystallogr., Sect. B: Struct. Sci.*, 1999, **55**, 627–663.

17 (*a*) K. Zhu, W. Jiang, Z. Wang, W. Li, W. Xie, H. Yang and W. Yang, *Angew. Chem., Int. Ed.*, 2023, **62**, e202213368; (*b*) K. Zhu, T. Wu and K. Huang, *ACS Nano*, 2019, **13**, 14447–14458.

18 (*a*) K. Zhu, H. Wang, W. Jiang, W. Xie, X. Li, Z. Jia and W. Yang, *Chem. Sci.*, 2023, **14**, 8889–8896; (*b*) K. Zhu, T. Wu, S. Sun, W. van den Bergh, M. Stefik and K. Huang, *Energy Storage Mater.*, 2020, **29**, 60–70.

19 (*a*) M. Yan, P. He, Y. Chen, S. Wang, Q. Wei, K. Zhao, X. Xu, Q. An, Y. Shuang, Y. Shao, K. T. Mueller, L. Mai, J. Liu and J. Yang, *Adv. Mater.*, 2018, **30**, 1703725; (*b*) K. Zhu, T. Wu and K. Huang, *Energy Storage Mater.*, 2021, **38**, 473–481; (*c*) X. Wang, Y. Li, S. Wang, F. Zhou, P. Das, C. Sun, S. Zheng and Z. S. Wu, *Adv. Energy Mater.*, 2020, **10**, 2000081.

20 (*a*) Z. Xing, G. Xu, J. Han, G. Chen, B. Lu, S. Liang and J. Zhou, *Trends Chem.*, 2023, **5**, 380–392; (*b*) X. Dou, X. Xie, S. Liang and G. Fang, *Sci. Bull.*, 2024, **69**, 833–845.

21 W. Li, W. Jiang, K. Zhu, Z. Wang, W. Xie, H. Yang, M. Ma and W. Yang, *Chem. Eng. J.*, 2024, **496**, 153786.

22 (*a*) J. Zhang, R. Liu, C. Huang, C. Dong, L. Xu, L. Yuan, S. Lu, L. Wang, L. Zhang and L. Chen, *Nano Energy*, 2024, **122**, 109301; (*b*) X. Wang, Y. Wang, A. Naveed, G. Li, H. Zhang, Y. Zhou, A. Dou, M. Su, Y. Liu, R. Guo and C. C. Li, *Adv. Funct. Mater.*, 2023, **33**, 2306205.

23 (*a*) Z. Xie, S. Liu, C. Wu, R. Cai, N. Li and S. Huang, *Energy Storage Mater.*, 2023, **60**, 102823; (*b*) G. Xu, X. Liu, S. Huang, L. Li, X. Wei, J. Cao, L. Yang and P. K. Chu, *ACS Appl. Mater. Interfaces*, 2020, **12**, 706–716; (*c*) P. He, G. Zhang, X. Liao, M. Yan, X. Xu, Q. An, J. Liu and L. Mai, *Adv. Energy Mater.*, 2018, **8**, 1702463.

24 Y. Qi, J. Huang, L. Yan, Y. Cao, J. Xu, D. Bin, M. Liao and Y. Xia, *Chem. Eng. J.*, 2022, **442**, 136349.

25 K. Zhu, T. Wu, W. van den Bergh, M. Stefik and K. Huang, *ACS Nano*, 2021, **15**, 10678–10688.

26 F. Ming, H. Liang, Y. Lei, S. Kandambeth, M. Eddaoudi and H. N. Alshareef, *ACS Energy Lett.*, 2018, **3**, 2602–2609.

27 (*a*) M. Li, M. Liu, Y. Lu, G. Zhang, Y. Zhang, Z. Li, Q. Xu, H. Liu and Y. Wang, *Adv. Funct. Mater.*, 2024, **34**, 2312789; (*b*) J. Huang, Z. Wang, M. Hou, X. Dong, Y. Liu, Y. Wang and Y. Xia, *Nat. Commun.*, 2018, **9**, 2906.

28 F. Wan, L. Zhang, X. Wang, S. Bi, Z. Niu and J. Chen, *Adv. Funct. Mater.*, 2018, **28**, 1804975.

29 (*a*) S. Liu, H. Zhu, B. Zhang, G. Li, H. Zhu, Y. Ren, H. Geng, Y. Yang, Q. Liu and C. C. Li, *Adv. Mater.*, 2020, **32**, e2001113; (*b*) W. Li, C. Han, Q. Gu, S. L. Chou, J. Z. Wang, H. K. Liu and S. X. Dou, *Adv. Energy Mater.*, 2020, **10**, 2001852; (*c*) Z. Wang, X. Tang, S. Yuan, M. Bai, H. Wang, S. Liu, M. Zhang and Y. Ma, *Adv. Funct. Mater.*, 2021, **31**, 2100164; (*d*) Y. Li, Y. Liu, J. Chen, Q. Zheng, Y. Huo, F. Xie and D. Lin, *Chem. Eng. J.*, 2022, **448**, 137681.

30 (*a*) F. S. Volkov, S. N. Eliseeva, M. A. Kamenskii, A. I. Volkov, E. G. Tolstopjatova, O. V. Glumov, L. Fu and V. V. Kondratiev, *Nanomaterials*, 2022, **12**, 3896; (*b*) T. Yang, D. Xin, N. Zhang, J. Li, X. Zhang, L. Dang, Q. Li, J. Sun, X. He, R. Jiang, Z. Liu and Z. Lei, *J. Mater. Chem. A*, 2024, **12**, 10137–10147.

31 (*a*) P. Hu, T. Zhu, J. Ma, C. Cai, G. Hu, X. Wang, Z. Liu, L. Zhou and L. Mai, *Chem. Commun.*, 2019, **55**, 8486–8489; (*b*) D. Kundu, B. D. Adams, V. Duffort, S. H. Vajargah and L. F. Nazar, *Nat. Energy*, 2016, **1**, 16119; (*c*) Q. Pang, C. Sun, Y. Yu, K. Zhao, Z. Zhang, P. M. Voyles, G. Chen, Y. Wei and X. Wang, *Adv. Energy Mater.*, 2018, **8**, 1800144; (*d*) V. Soundharrajan, B. Sambandam, S. Kim, M. H. Alfaruqi, D. Y. Putro, J. Jo, S. Kim, V. Mathew, Y. K. Sun and J. Kim, *Nano Lett.*, 2018, **18**, 2402–2410; (*e*) B. Sambandam, V. Soundharrajan, S. Kim, M. H. Alfaruqi, J. Jo, S. Kim, V. Mathew, Y.-k. Sun and J. Kim, *J. Mater. Chem. A*, 2018, **6**, 15530–15539; (*f*) N. Zhang, F. Cheng, J. Liu, L. Wang, X. Long, X. Liu, F. Li and J. Chen, *Nat. Commun.*, 2017, **8**, 405.

32 K. Zhu, T. Wu and K. Huang, *Chem. Mater.*, 2021, **33**, 4089.

33 W. Jiang, K. Zhu, W. Xie, Z. Wang, Z. Ou and W. Yang, *Chem. Sci.*, 2024, **15**, 2601–2611.